

Characterisation of the non-Gaussianity of radio and IR point sources at CMB frequencies

F. Lacasa^{1*}, N. Aghanim¹, M. Kunz², and M. Frommert²

¹ *Institut d’Astrophysique Spatiale (IAS), Bâtiment 121, F-91405 Orsay (France); Université Paris-Sud 11 and CNRS (UMR 8617)*

² *Département de Physique Théorique and Center for Astroparticle Physics, Université de Genève, 24 quai E. Ansermet, Genève*

ABSTRACT

The present study focuses on the characterisation of the non-Gaussianity produced by radio point sources and, for the first time, by infrared sources in the frequency range of the CMB from 30 to 350 GHz.

We propose a simple prescription to infer the bispectrum from the power spectrum for point sources considering different independent populations of sources, with or without clustering. We test the accuracy of our prediction using publicly available all-sky simulations of radio and IR sources and find very good agreement.

We further characterise the configuration dependence and the frequency behaviour of the IR and radio bispectra. We show that the IR bispectrum peaks for squeezed triangles and that the clustering of IR sources enhances the bispectrum values by several orders of magnitude at scales $\ell \sim 100$. At 150 GHz the bispectrum of IR sources starts to dominate over that of radio sources on large angular scales, and it dominates over the whole multipole range at 350 GHz.

Finally, we compute the bias on f_{NL} induced by radio and IR sources. We show that the positive bias induced by radio sources is significantly reduced by masking the sources. We also show, for the first time, that the form of the IR bispectrum mimics a primordial ‘local’ bispectrum f_{NL} . The IR sources produce a negative bias which becomes important for Planck-like resolution and at high frequencies ($\Delta f_{\text{NL}} \sim -6$ at 277 GHz and $\Delta f_{\text{NL}} \sim -60-70$ at 350 GHz). Most of the signal being due to the clustering of faint IR sources, the bias $\Delta f_{\text{NL}}^{\text{IR}}$ is not reduced by masking sources above a flux limit and may, in some cases, even be increased due to the reduction of the shot-noise term.

Key words: Cosmology: Cosmic Microwave Background, large scale structures; Galaxies: statistics, Infrared: galaxies; Radio continuum: galaxies; Methods: statistical

1 INTRODUCTION

In the last decades, the Cosmic Microwave Background (CMB) has become a very successful probe of the early and late universe. The smallness of the perturbations in the metric and in the cosmic fluids allows us to use linear perturbation theory to compute their evolution efficiently and accurately through Boltzmann codes (Seljak & Zaldarriaga (1996), Lewis et al. (2000), Lesgourgues (2011)).

Since COBE (Smoot et al. 1992) the measurement of the CMB power spectrum has been achieved by many experiments and over a wide range of scales. The most recent CMB data are those of WMAP (Larson et al. 2011), ACT (Barrientos et al. 2010) and SPT (Keisler et al. 2011). Constraints from all these measurements, combined with other probes, e.g BAO (Percival et al. 2010), SN-Ia (Hicken et al.

2009) and H_0 (Riess et al. 2009) measurements, give a converging view of our Universe and have led to the establishment of a ‘standard model’ of cosmology (e.g Larson et al. (2011)) known as Λ CDM. In this model, the universe is flat, dominated by a cold dark matter component and a ‘dark energy’ component compatible with a cosmological constant. The present constraints suggest that CMB anisotropies are a realisation of a primordial random process that generated the initial perturbations from quantum fluctuations which were then stretched to macroscopic scales by inflation (Liddle & Lyth 2000).

The microwave sky is however not made of CMB primary signal alone, it consists also of secondary anisotropies such as those associated with the Integrated Sachs-Wolfe effect, those arising from the Sunyaev-Zel’dovich (SZ) effect (inverse Compton scattering) in the direction of galaxy clusters, those due to Doppler effect from moving structures (e.g. kinetic SZ effect from clusters and reionisation

* E-mail: Fabien.Lacasa@ias.u-psud.fr

patches), see Aghanim et al. (2008) for details. In addition, there are other astrophysical components in the microwave domain such as the dust, synchrotron and free-free emissions from our Galaxy, the emission from radio sources that dominate at lower frequencies but contribute significantly at microwave frequencies, and the emission from dusty star forming galaxies emitting mainly in the Infra-Red (IR) domain (Low & Tucker 1968).

In the present study, we will focus only on the characterisation of the extra-Galactic point sources, namely the radio sources and the IR dusty galaxies. They contribute notably to the power spectrum at CMB frequencies and start dominating over the CMB at about $\ell \sim 2000$. Active Galactic Nuclei (AGN) are observed as radio sources via their synchrotron emission. They have been widely studied in the CMB context especially at low frequencies $\nu \leq 90$ GHz (de Zotti et al. 2005). They affect mostly the lower end of frequencies observed by CMB experiments. Their largest impact was thought to be in the frequency bands from 30 to 90 GHz but the recent Planck results (Planck-Collaboration 2011c,a) show that radio sources are detected at frequencies as high as 217 GHz. At the CMB frequencies, radio sources do not cluster and thus exhibit a flat power-spectrum.

Star-forming galaxies are observed as IR sources via the thermal emission from dust heated by the ultra-violet emission of stars. These IR sources contribute to the signal observed by CMB experiments at frequencies higher than 150 GHz, thus being particularly relevant for the most recent CMB experiments, e.g. SPT, ACT and Planck High Frequency Instrument observations. The cumulated emission from the IR sources, the Cosmic Infrared Background (CIB), was first discovered by Puget et al. (1996), and its anisotropies were first characterised by Lagache & Puget (2000) and Matsuhara et al. (2000). Many other observations were possible in the last decade in the IR and submm domain (Lagache et al. (2007), Viero et al. (2009), Hall et al. (2010), Amblard et al. (2011), Planck-Collaboration (2011d)). In particular, the latest constraints of the CIB from Planck showed that its power spectrum, at frequencies 217-353-545-857 GHz, is well modeled by a power law $C_{\ell}^{\text{CIB}}(\nu) = A(\nu) \times \left(\frac{\ell}{1000}\right)^n$ with e.g. $A = (104 \pm 4) \times 10^2 \text{Jy}^2/\text{sr}$ and $n = -1.08 \pm 0.06$ at 545 GHz. This behaviour contrasts with the flat spectrum of radio sources and is due to the clustering of the IR galaxies and their host dark-matter halos.

These point sources are super-imposed on the primordial fluctuations. The simplest models of inflation (single-field and slow-roll) predict a small primordial non-Gaussianity (NG) (Maldacena (2003), Creminelli & Zaldarriaga (2004)) that is sub-dominant to the NG induced by the non-linear evolution of the perturbations, a contribution that is necessarily always present. More complex inflationary models, e.g. multi-field scenarios, may predict larger NG (Byrnes & Choi 2010), to the point of being detectable. A simple and yet powerful probe of non-Gaussianity is the three-point function in harmonic space, the bispectrum (see section 2 for more details), which is defined as a function of a multipole triplet (ℓ_1, ℓ_2, ℓ_3) . The bispectrum vanishes for a Gaussian field like all odd-order moments. Besides the bispectrum, connected even-order moments may also be used to probe non-Gaussianity, and the 4-point function or trispec-

trum has indeed been a focus of interest (Kunz et al. 2001), especially for lensing studies (Cooray & Kesden 2002).

There are many different models of inflation, and they often predict very similar power spectra that are close to scale invariant. For models that lead to a measurable bispectrum, however, this degeneracy can often be broken by studying the dependence of the bispectrum amplitude on (ℓ_1, ℓ_2, ℓ_3) , e.g. a large signal for squeezed triangles is indicative of slow-roll multi-field inflation models, equilateral triangles are enhanced for models with non-canonical kinetic terms, and folded triangles for non-standard vacuum initial conditions. The most studied and constrained form of non-Gaussianity is the local ansatz parametrised by a factor f_{NL} , and predicted by several inflation models. Current constraints on local non-Gaussianity show that the CMB is consistent with being Gaussian at the 95% C.L. (Komatsu et al. 2011), and constraints on other shapes all show consistency with Gaussianity as well.

Given the current limits on primordial NG, astrophysical signals are the dominant contribution to non-Gaussianity. While Galactic emission and resolved sources may be accounted for by masking, unresolved sources and residuals have to be characterised. As opposed to primordial NG, radio sources NG has been detected, and was studied for the WMAP mission showing that it yields a non-zero flat bispectrum parametrised as b_{src} or b_{ps} . The WMAP5 best estimate in the Q band is $b_{\text{src}} = 4.3 \pm 1.3 \mu\text{K}^3 \text{sr}^2$ (Komatsu et al. 2009). Characterising the NG signal from astrophysical components and more importantly from extra-Galactic point sources is important for two main reasons: (i) to avoid mistaking it for a primordial contribution (and to allow the development of robust methods to isolate primordial NG) and (ii) to learn more about astrophysical processes, i.e. go beyond the description of point sources by their number counts and their power spectrum.

The study of NG from extra-Galactic point sources has been pioneered by Argueso et al. (2003), focusing mostly on the radio sources and including clustering. They showed that the point-source bispectrum is mostly flat at WMAP frequencies and dominates the CMB bispectrum in most configurations. Babich & Pierpaoli (2008) investigated the bias on the f_{NL} estimator induced by radio sources, considering the modulation of their number density with ISW, of their magnification with lensing and of the flux cut-off with selection effects. Serra & Cooray (2008) studied the bias on f_{NL} due to radio sources, SZ-lensing and ISW-lensing bispectra, investigating the dependence of this bias with the resolution scale. Finally Munshi et al. (2009) defined skew-spectra for cross-correlation analysis and their estimator and applied it to secondary anisotropies.

In this paper we study the non-Gaussianity produced by infrared and radio point sources in the frequency range of the CMB from 30 to 350 GHz, based on numerical simulations by Sehgal et al. (2010). We investigate the frequency and configuration dependence of the bispectrum. We particularly focus on the non-Gaussianity from IR sources and their clustering term. We restrict the study to the simplest case of full sky maps without masks. Furthermore, we do not take into account noise and beam effects. Statistical isotropy of all fields considered will be assumed throughout this article. The case of noisy, partially masked maps will be addressed in future studies.

In section 2 we review the estimator of the (binned) bispectrum and f_{NL} and develop a parametrisation of the bispectrum to display and visualise it efficiently. In section 3, we develop a prescription to infer the bispectrum from the power spectrum for clustered sources and for different populations. In section 4 we use available full-sky simulations of radio and infrared sources to compute and characterise their bispectrum at CMB frequencies and we compare these bispectra to the predictions of the prescription. We examine the configuration dependence of the point-source bispectra with the parametrisation and study the bias they induce on the estimation of primordial local non-Gaussianity in Sect. 5. We finally conclude and discuss our results in section 6.

2 THREE-POINT NG ESTIMATORS

2.1 Full-sky bispectrum estimator

Given a full-sky map of the temperature fluctuations $\Delta T(\mathbf{n})$ of some signal, it can be decomposed in the spherical harmonic basis

$$a_{\ell m} = \int d^2\mathbf{n} Y_{\ell m}^*(\mathbf{n}) \Delta T(\mathbf{n}) \quad (1)$$

with the usual orthonormal spherical harmonics $Y_{\ell m}$

$$\int d^2\mathbf{n} Y_{\ell m}(\mathbf{n}) Y_{\ell' m'}^*(\mathbf{n}) = \delta_{\ell\ell'} \delta_{mm'}.$$

Observational data is pixelised, so that the integral is replaced by a sum over pixels. We will assume that the solid angle of a pixel, Ω_{pix} , is constant, which is for example the case for the HEALPix¹ pixelisation scheme that we will adopt for the numerical calculations. In this case we have that

$$a_{\ell m} = \sum_{\mathbf{n}_i} Y_{\ell m}^*(\mathbf{n}_i) \Delta T(\mathbf{n}_i) \Omega_{\text{pix}} \quad (2)$$

This discreteness effect will be important e.g in section 3.1.

In order to compute the bispectrum, equivalent to the 3-point correlation function in the harmonic space, we will resort to scale-maps as defined by Spergel & Goldberg (1999) and also used by Aghanim et al. (2003) and De Troia et al. (2003),

$$T_{\ell}(\mathbf{n}) = \sum_m a_{\ell m} Y_{\ell m}(\mathbf{n}) = \int d^2\mathbf{n}' T(\mathbf{n}') P_{\ell}(\mathbf{n} \cdot \mathbf{n}') \quad (3)$$

The optimal bispectrum estimator is then

$$\hat{b}_{\ell_1 \ell_2 \ell_3} = \frac{4\pi}{(2\ell_1 + 1)(2\ell_2 + 1)(2\ell_3 + 1)} \begin{pmatrix} \ell_1 & \ell_2 & \ell_3 \\ 0 & 0 & 0 \end{pmatrix}^{-2} \times \int d^2\mathbf{n} T_{\ell_1}(\mathbf{n}) T_{\ell_2}(\mathbf{n}) T_{\ell_3}(\mathbf{n}) \quad (4)$$

or it can be written in the form:

$$\hat{b}_{\ell_1 \ell_2 \ell_3} = \sqrt{\frac{4\pi}{(2\ell_1 + 1)(2\ell_2 + 1)(2\ell_3 + 1)}} \begin{pmatrix} \ell_1 & \ell_2 & \ell_3 \\ 0 & 0 & 0 \end{pmatrix}^{-1} \times \sum_{m_1, m_2, m_3} \begin{pmatrix} \ell_1 & \ell_2 & \ell_3 \\ m_1 & m_2 & m_3 \end{pmatrix} a_{\ell_1 m_1} a_{\ell_2 m_2} a_{\ell_3 m_3}$$

Equation (5) is computationally expensive when implemented at high ℓ due to the high number of Wigner symbols to calculate. Equation 4 still requires a few cpu-days for a full computation at a Planck-like resolution, $N_{\text{side}}=1024 - 2048$. Binning the multipoles in ℓ , as Bucher et al. (2010), has the advantage of speeding up the computations and smoothing out the variations due to cosmic variance.

For a given triangle in harmonic space (ℓ_1, ℓ_2, ℓ_3) the number of independent configurations on the sphere is:

$$N_{\ell_1 \ell_2 \ell_3} = \frac{(2\ell_1 + 1)(2\ell_2 + 1)(2\ell_3 + 1)}{4\pi} \begin{pmatrix} \ell_1 & \ell_2 & \ell_3 \\ 0 & 0 & 0 \end{pmatrix}^2 \quad (6)$$

When multipoles are binned in bins of width $\Delta\ell$ the expression for the scale-maps (Eq. 3) becomes:

$$T_{\Delta\ell}(\mathbf{n}) = \sum_{\ell \in \Delta\ell, m} a_{\ell m} Y_{\ell m}(\mathbf{n}) \quad (7)$$

and a binned bispectrum estimator identically weighting triangles is given by:

$$\hat{b}_{\Delta\ell_1, \Delta\ell_2, \Delta\ell_3} = \frac{1}{N_{\Delta}(\Delta\ell_1, \Delta\ell_2, \Delta\ell_3)} \int d^2\mathbf{n} T_{\Delta\ell_1}(\mathbf{n}) T_{\Delta\ell_2}(\mathbf{n}) T_{\Delta\ell_3}(\mathbf{n}) \quad (8)$$

where

$$N_{\Delta}(\Delta\ell_1, \Delta\ell_2, \Delta\ell_3) = \sum_{\ell_i \in \Delta\ell_i} N_{\ell_1 \ell_2 \ell_3}$$

One can easily check that the obtained binned bispectrum estimator is unbiased for a constant bispectrum and that the bias can be neglected as long as the bispectrum does not vary significantly within a bin $\Delta\ell$. In the following, we have chosen $\Delta\ell = 64$ for the bin width.

2.2 f_{NL} estimator

The most studied and constrained form of non-Gaussianity is the local ansatz parametrised by a factor f_{NL} :

$$\Phi(x) = \Phi_G(x) + f_{\text{NL}} (\Phi_G^2(x) - \langle \Phi_G^2(x) \rangle) \quad (9)$$

where $\Phi(x)$ is the Bardeen potential and $\Phi_G(x)$ is a Gaussian field. This form of NG yields the following CMB bispectrum (Komatsu & Spergel 2001):

$$b_{\ell_1 \ell_2 \ell_3}^{\text{loc}} = \int r^2 dr \alpha_{\ell_1}(r) \beta_{\ell_2}(r) \beta_{\ell_3}(r) + \text{perm.} \quad (10)$$

with

$$\alpha_{\ell}(r) = \frac{2}{\pi} \int k^2 dk g_{T,\ell}(k) j_{\ell}(kr) \quad (11)$$

$$\beta_{\ell}(r) = \frac{2}{\pi} \int k^2 dk P(k) g_{T,\ell}(k) j_{\ell}(kr) \quad (12)$$

where $g_{T,\ell}$ is the radiation transfer function, which can be computed with a Boltzmann code, j_{ℓ} are the spherical Bessel functions, and $P(k) \propto k^{n_s-4}$ is the primordial power spectrum, with a spectral index n_s .

On large angular scales, the Sachs-Wolfe (SW) effect is the dominant contribution to the CMB signal. In this regime, the CMB bispectrum takes the following analytical form:

$$b_{\ell_1 \ell_2 \ell_3}^{\text{loc}} \propto - \left(\frac{1}{\ell_1^2 \ell_2^2} + \frac{1}{\ell_1^2 \ell_3^2} + \frac{1}{\ell_2^2 \ell_3^2} \right) \quad (13)$$

¹ <http://healpix.jpl.nasa.gov>

This bispectrum is maximal when one of the multipoles is minimal ($\ell_1 \ll \ell_2 \simeq \ell_3$) which is called the squeezed configuration.

A commonly used cubic estimator of f_{NL} has been developed by Komatsu et al. (2005). It is much faster than performing the whole bispectrum analysis and fitting the local bispectrum. In its original version, the estimator takes into account beam profile and homogeneous noise, and has been used on WMAP data to yield the current constraint $-10 < f_{\text{NL}} < 74$ (Komatsu et al. 2011). The estimator was then further developed by several authors by adding a linear term accounting for masking and inhomogeneous noise (Creminelli et al. 2006). Here, we will only consider noiseless full-sky maps without beam smoothing so that we can apply the estimator in its original form.

To build the f_{NL} estimator we first define the filtered maps at comoving distance r and direction \mathbf{n} :

$$A(r, \mathbf{n}) = \sum_{\ell m} \frac{\alpha_{\ell}(r)}{C_{\ell}} a_{\ell m} Y_{\ell m}(\mathbf{n}) \quad (14)$$

$$B(r, \mathbf{n}) = \sum_{\ell m} \frac{\beta_{\ell}(r)}{C_{\ell}} a_{\ell m} Y_{\ell m}(\mathbf{n}) \quad (15)$$

where C_{ℓ} is the CMB power spectrum. $B(r, \mathbf{n})$ is then an estimated map of the primordial potential fluctuations $\Phi(r, \mathbf{n})$ via Wiener filtering.

The integral of AB^2 permits us to estimate f_{NL} as:

$$\hat{f}_{\text{NL}} \sum_{\ell_1 \leq \ell_2 \leq \ell_3} \frac{(B_{\ell_1 \ell_2 \ell_3}^{\text{loc}})^2}{C_{\ell_1} C_{\ell_2} C_{\ell_3}} = \int r^2 dr d^2 \mathbf{n} A(r, \mathbf{n}) B^2(r, \mathbf{n}) \quad (16)$$

where $B_{\ell_1 \ell_2 \ell_3}^{\text{loc}} = \sqrt{N_{\ell_1 \ell_2 \ell_3}} b_{\ell_1 \ell_2 \ell_3}^{\text{loc}}$ is the local bispectrum for $f_{\text{NL}} = 1$, to be compared with the observed value $B_{\ell_1 \ell_2 \ell_3}^{\text{obs}}$. It can be shown that this estimator takes analytically the form:

$$\hat{f}_{\text{NL}} = \frac{\sum_{\ell_1 \leq \ell_2 \leq \ell_3} \frac{B_{\ell_1 \ell_2 \ell_3}^{\text{obs}} B_{\ell_1 \ell_2 \ell_3}^{\text{loc}}}{C_{\ell_1} C_{\ell_2} C_{\ell_3}}}{\sum_{\ell_1 \leq \ell_2 \leq \ell_3} \frac{(B_{\ell_1 \ell_2 \ell_3}^{\text{loc}})^2}{C_{\ell_1} C_{\ell_2} C_{\ell_3}}} \quad (17)$$

It is near-optimal in the sense that it minimizes the χ^2 for weak NG (under some assumptions on isosceles and equilateral triangles). The estimator becomes sub-optimal (e.g. Elsner & Wandelt (2009)) for large enough f_{NL} , when the variance of the bispectrum gets $O(f_{\text{NL}}^2)$ correction compared to the weak NG computation with Wick's theorem.

2.3 Parametrisation of the bispectrum

Several ways of visualising the bispectrum have been proposed in the literature, e.g. isosurfaces in the (ℓ_1, ℓ_2, ℓ_3) 3D space by Fergusson & Liguori (2010), or slices of constant perimeter in the orthogonal transverse coordinate $(\ell_{\perp a}, \ell_{\perp b})$ space by Bucher et al. (2010).

Under the assumption of statistical isotropy, the bispectrum $b_{\ell_1 \ell_2 \ell_3}$ is invariant under permutations of ℓ_1, ℓ_2 and ℓ_3 , i.e. it is a function of the shape and size of the triangle (ℓ_1, ℓ_2, ℓ_3) only, i.e. independent of its orientation. Therefore, we can find a parametrisation invariant under permutation of ℓ_1, ℓ_2 , and ℓ_3 , which avoids redundancy of information and allows convenient visualisation and interpretation of data. Let us denote as $(\bar{\ell}_1, \bar{\ell}_2, \bar{\ell}_3)$ the equivalence class of the triplet under permutations.

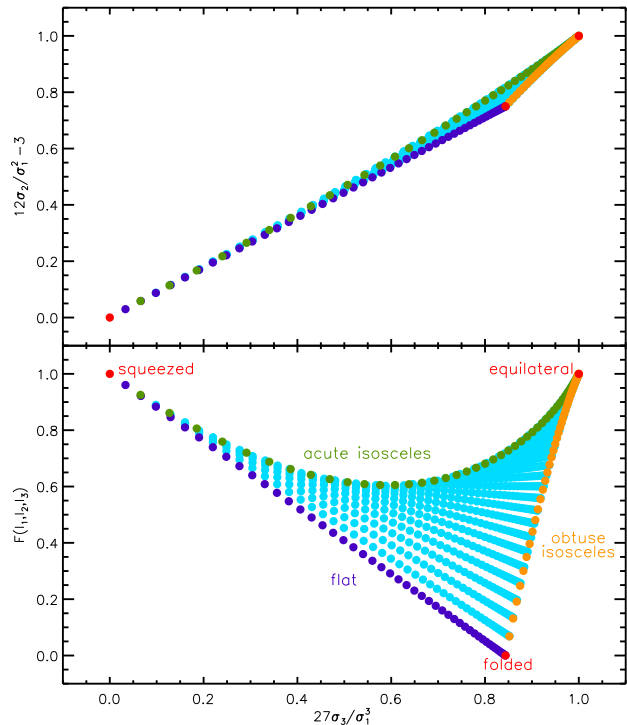


Figure 1. Triangles of constant perimeter, P , in the parametrisation defined by the normalised symmetric polynomials (upper panel), or in the parameter space (F, S) defined in the text (bottom panel).

The elementary symmetric polynomials ensure the invariance under permutations:

- $\sigma_1 = \ell_1 + \ell_2 + \ell_3$
- $\sigma_2 = \ell_1 \ell_2 + \ell_1 \ell_3 + \ell_2 \ell_3$
- $\sigma_3 = \ell_1 \ell_2 \ell_3$

Through Cardan's formula, there is a one-to-one correspondence between $(\bar{\ell}_1, \bar{\ell}_2, \bar{\ell}_3)$, defined by the roots of the polynomial $X^3 - \sigma_1 X^2 + \sigma_2 X - \sigma_3$, and the triplet $(\sigma_1, \sigma_2, \sigma_3)$. We further define the scale-invariant parameters $\tilde{\sigma}_2 = 12\sigma_2/\sigma_1^2 - 3$ and $\tilde{\sigma}_3 = 27\sigma_3/\sigma_1^3$ with coefficient chosen so that $\tilde{\sigma}_2$ and $\tilde{\sigma}_3$ vary in the range $[0, 1]$. As illustrated in the upper panel of Fig. 1, this parametrisation does not allow us to discriminate efficiently between the different triangles.

We find that the parameters noted (P, F, S) and defined as:

- $P = \sigma_1$
- $F = 32(\tilde{\sigma}_2 - \tilde{\sigma}_3)/3 + 1$
- $S = \tilde{\sigma}_3$

provide a clearer distinction of the triangles as is illustrated in the bottom panel of Fig. 1.

To illustrate the use of our (P, F, S) -parametrisation, we plot in Fig. 2² the theoretical CMB bispectrum produced by the local NG model f_{NL} , computed through Eq. 10. The triangle perimeters, P , vary between $P_{\text{min}} = 30$ (equilateral

² For space reasons we only include some of the bins in the figures in the paper. Full resolution plots with all perimeter bins are available upon request.

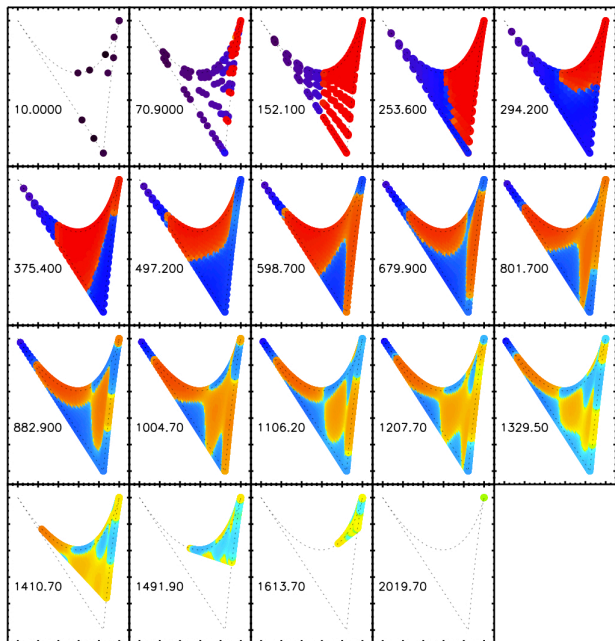


Figure 2. Theoretical CMB bispectrum produced by the local model in the (P, F, S) -parametrisation. With chosen representative perimeters and asinh color scale from deep purple/black (most negative) to red/dark grey (positive). $P/3$ is given on each panel.

configuration with $\ell_{\min} = 10$) and $P_{\max} = 6120$ (equilateral configuration with $\ell_{\max} = 2040$). We plot representative perimeters tracing the building up of the bispectrum with scale, giving $P/3$ on each panel. The color code scales from deep purple/black (most negative) to red/dark grey (positive).

In the first panels for the smallest perimeters, few triangles are present. As the perimeter increases the (F, S) space is populated starting with equilateral configurations (upper right corner) first to reach squeezed configuration (upper left corner) later. Conversely in the last panels for the largest perimeters, the resolution limit $\ell_{\max} = 2048$ limits the possible configurations, leaving only the equilateral triangles in the end.

The Sachs-Wolfe shape (see Eq. 13) is visible at low perimeters, with the colors (value of the bispectrum) varying horizontally with S but not vertically with F . We note that the strong negative values (deep purple/black) are located in the near-squeezed configuration (upper left corner). The sign of the radiation transfer function can be traced via the equilateral triangles which are positive for $P/3 \sim 200$ (first acoustic peak) and become negative for $P/3 \sim 500$ (second acoustic peak) etc. The squeezed configuration in turn is always negative as the smallest multipole has negative transfer function via SW. The folded configuration has relatively large negative values when the two smallest multipoles are in the first acoustic peak while the biggest multipole is in the second acoustic peak ($P \sim 900 - 1200 \Rightarrow P/3 \sim 300 - 400$). For larger perimeters the structure becomes complex as several acoustic peaks intervene.

3 PHYSICAL PRESCRIPTION FOR THE POINT-SOURCE BISPECTRUM

In this section we develop a prescription which permits us to predict the (bi)spectrum of point sources, starting from the simplest case of a single randomly-distributed population to the case of multiple clustered populations. This is a situation that is encountered in current and future CMB analyses. Indeed until recently, CMB experiments have focussed on frequencies where unclustered radio sources are the only dominant kind of point sources, but the CMB is also non-negligible at higher frequencies where an independent population of dusty galaxies becomes important together with the SZ signal of clusters. This is of particular relevance for Planck which has a large frequency range covering both populations.

3.1 Single source population: shot-noise contribution

A source with flux S enclosed in a pixel with solid angle Ω_{pix} yields a temperature variation $\Delta T = k_{\nu} \frac{S}{\Omega_{\text{pix}}}$, where $k_{\nu} = \left. \frac{\partial B(\nu, T)}{\partial T} \right|_{T_{\text{CMB}}}$, $B(\nu, T)$ is the black-body spectrum and T_{CMB} is the CMB mean temperature.

As shown in Appendix A the power spectrum of a source population is given by:

$$C_{\ell} = C_{\ell}^{\text{clust}} + C_{\ell}^{\text{shot}} \quad (18)$$

The discreteness of the sources produces a constant-term spectrum C_{ℓ}^{shot} which is usually named ‘Poissonian’ because the number of unclustered point sources is driven a priori by Poisson statistics (Sehgal et al. 2010). The shot-noise term reads:

$$C_{\ell}^{\text{shot}} = \frac{k_{\nu}^2}{4\pi} \times \int S^2 \frac{dn}{dS} dS \quad (19)$$

where $\frac{dn}{dS}$ are the number counts of sources and the integral is performed from 0 to S_{cut} , the detection limit, i.e. only sources with $S > S_{\text{cut}}$ are detected, the rest being unresolved.

The discreteness property of sources, when computing the three-point correlation function, yields a statistically isotropic bispectrum constant with ℓ :

$$b_{\ell_1 \ell_2 \ell_3}^{\text{shot}} = \frac{k_{\nu}^3}{4\pi} \times \int S^3 \frac{dn}{dS} dS \quad (20)$$

for $\ell_i \neq 0$. Equations (18), (19) and (20) are derived in more detail in Appendix A.

The case of sources randomly and independently distributed on the sky is that of the radio sources at CMB frequencies. The correlation vanishes and the total (bi)spectrum is equal to the shot-noise (bi)spectrum. The distribution of the sources is that of a white-noise entirely characterised by the one-point probability distribution. In this case, Eqs. (19) and (20) for the shot noise contribution can be reformulated simply in terms of temperature variations where the white-noise spectrum and bispectrum are related to the variance σ^2 and skewness κ_3 of ΔT :

$$C_{\ell}^{\text{white}} = \sigma^2 \Omega_{\text{pix}} \quad (21)$$

$$b_{\ell_1 \ell_2 \ell_3}^{\text{white}} = \kappa_3 \Omega_{\text{pix}}^2 \quad (22)$$

with $\sigma^2 = \langle (\Delta T - \langle \Delta T \rangle)^2 \rangle$ and $\kappa_3 = \langle (\Delta T - \langle \Delta T \rangle)^3 \rangle$

3.2 Single source population with correlations

The effect of clustering of a single population of sources, namely radio sources, on the bispectrum was pioneered by Argueso et al. (2003) who proposed a prescription to address this issue. The elements entering the prescription are the number counts of sources and a theoretical or observational correlation function $w(\theta)$. Defining

$$P(k)_{\text{clust}} = 2\pi \int w(\theta) J_0(k\theta) d\theta \quad (23)$$

where θ is the distance on the flat patch and J_0 the Bessel function, the prescription is:

$$\delta_{\vec{k}}(\text{tot}) = \sqrt{\frac{P(k)_{\text{clust}} + P(k)_{\text{shot}}}{P(k)_{\text{white}}}} \times \delta_{\vec{k}}(\text{white}) \quad (24)$$

where $\delta_{\vec{k}}$ are the Fourier coefficient of the map, ‘shot’ and ‘white’ refer respectively to the shot-noise and white-noise process. Then Argueso et al. compute the bispectrum from simulated square maps based on their prescription.

In our study, we have extended the above-described prescription to analytically derive the full-sky bispectrum. The full-sky scale-maps read:

$$T_{\ell}^{\text{tot}}(\mathbf{n}) = \sqrt{\frac{C_{\ell}^{\text{clust}} + C_{\ell}^{\text{shot}}}{C_{\ell}^{\text{white}}}} \times T_{\ell}^{\text{white}}(\mathbf{n})$$

which reduces to Eq. (24) in the flat-sky approximation $\ell = 2\pi k$, and assuming $P(k)$ does not vary much within a k bin. So the power spectrum is given by:

$$C_{\ell}^{\text{tot}} = C_{\ell}^{\text{clust}} + C_{\ell}^{\text{shot}}.$$

We remind the reader that the Argueso et al.’s prescription is specifically made to meet the above relation, and that $C_{\ell}^{\text{shot}} = C_{\ell}^{\text{white}} = \text{const.}$

More interestingly the bispectrum is found to be:

$$\begin{aligned} b_{\ell_1 \ell_2 \ell_3}^{\text{tot}} &= \sqrt{1 + \frac{C_{\ell_1}^{\text{clust}}}{C_{\ell_1}^{\text{white}}}} \sqrt{1 + \frac{C_{\ell_2}^{\text{clust}}}{C_{\ell_2}^{\text{white}}}} \sqrt{1 + \frac{C_{\ell_3}^{\text{clust}}}{C_{\ell_3}^{\text{white}}}} \\ &\quad \times b_{\ell_1 \ell_2 \ell_3}^{\text{white}} \quad (25) \\ &\propto \sqrt{C_{\ell_1}^{\text{tot}} C_{\ell_2}^{\text{tot}} C_{\ell_3}^{\text{tot}}} \end{aligned}$$

with $b_{\ell_1 \ell_2 \ell_3}^{\text{white}} = \text{const.}$

Equation (25) of the bispectrum relates to the clustered power spectrum, or conversely the correlation function entering in the prescription.

3.3 Two populations of sources with clustering

The previous prescription, Eq. (24), describes well a single point source population. However, it fails at describing the cases where more than one population contribute to the signal. In particular, the case of the present generation of CMB experiments observing the CMB from low (30 GHz) to high (860 GHz) frequencies calls for an appropriate prescription which deals with independent source populations. Indeed, early results from the Planck mission (Planck-Collaboration 2011b) (Planck-Collaboration 2011a) show that radio and IR galaxies both contribute at frequencies of 100 GHz and

above. In the following we thus extend and generalise the prescription accordingly.

We hence define the harmonic coefficients as:

$$a_{\ell m}^{(\text{tot})} = a_{\ell m}^{(\text{white},1)} + \sqrt{\frac{C_{\ell}^{\text{clust}} + C_{\ell}^{\text{shot}}}{C_{\ell}^{\text{white},2}}} \times a_{\ell m}^{(\text{white},2)} \quad (26)$$

where $a_{\ell m}^{(\text{white},1)}$ and $a_{\ell m}^{(\text{white},2)}$ are independent realisations of white-noise with different number counts. Index 1 refers to the radio population and 2 to the infrared population. The spectrum has then a form similar to the case of a single source population:

$$C_{\ell} = C_{\ell}^{\text{clust}} + C_{\ell}^{\text{shot},1+2}$$

But the bispectrum differs, and reads:

$$b_{\ell_1 \ell_2 \ell_3}^{\text{tot}} = b_{\ell_1 \ell_2 \ell_3}^{\text{white},1} + \sqrt{\frac{C_{\ell_1}^{\text{tot},2}}{C_{\ell_1}^{\text{white},2}} \frac{C_{\ell_2}^{\text{tot},2}}{C_{\ell_2}^{\text{white},2}} \frac{C_{\ell_3}^{\text{tot},2}}{C_{\ell_3}^{\text{white},2}}} \times b_{\ell_1 \ell_2 \ell_3}^{\text{white},2} \quad (27)$$

For illustration, let us compare equations (25) and (27) in the equilateral configuration with white-noises of both populations derived from the same number counts, and neglecting the shot-noise of the second population:

$$b_{\ell \ell \ell}^{\text{1pop}} = \left(1 + \frac{C_{\ell}^{\text{clust}}}{C_{\ell}^{\text{white}}}\right)^{3/2} b_{\ell \ell \ell}^{\text{white}} \quad (28)$$

$$b_{\ell \ell \ell}^{\text{2pop}} = \left(1 + \left(\frac{C_{\ell}^{\text{clust}}}{C_{\ell}^{\text{white}}}\right)^{3/2}\right) b_{\ell \ell \ell}^{\text{white}} \quad (29)$$

The difference between these two formula is maximal when $C_{\ell}^{\text{clust}}/C_{\ell}^{\text{white}} \simeq 1$ and can be up to 40%, illustrating the need to properly account for the different populations.

The two-population case, representative of the CMB context in the frequency range of interest, can be straightforwardly generalised to more point-source populations with or without clustering properties.

4 RESULTS

In this section we present the bispectra of radio and IR sources computed on simulations described below, showing the configuration dependence of the bispectrum and its frequency behaviour.

4.1 Data used

For our analysis, we used the all-sky simulated maps³ of the IR and radio point sources provided by Sehgal et al. (2010) at 30, 90, 148, 219 and 350 GHz. We provide here a brief summary of the map construction. For the detailed description, we refer the reader to the above-cited article. The maps are based on N-body simulations of the large scale structure, with a volume 1000 h⁻¹Mpc on a side, produced using a tree-particle mesh code. Dark matter (DM) haloes are identified and are then populated with infrared and radio galaxies. The model for the radio sources is adapted so that

³ The frequency maps are available on Lambda website, http://lambda.gsfc.nasa.gov/toolbox/tb_cmbstim.ov.cfm

the radio luminosity function matches that of the observed radio sources at 151 MHz.

The IR-source model was partially based on Righi et al. (2008). The DM haloes are populated with galaxies of given luminosities taking into account a Poisson term and a correlation term. The model was constructed so that it is compatible with constraints on the luminosity function, the source counts and the fluctuations from SCUBA, BLAST, Spitzer and ACBAR (see Sehgal et al. (2010) for details). However, the simulation of IR sources, used here, does not account for the most recent observational constraints from ACT, SPT Herschel and Planck results.

Maps of the different astrophysical contributions, in HEALPix format at $N_{\text{side}}=8192$, were produced by replication of one simulated octant of the sky. This procedure does not properly account for the signal at the largest scales especially up to the octopole, $\ell = 3$; it also introduces excess power at $\ell \leq 300$ for infrared sources as discussed by Sehgal et al. (2010), but the power is correct for higher multipoles. The produced maps have half-arcminute resolution but we degraded them to $N_{\text{side}}=1024$ and used a uniform binning $\Delta\ell = 64$, to speed up computations. We checked that this procedure does not introduce a bias by comparing the binned spectrum in the degraded map to the unbinned spectrum in the original map and find excellent agreement. The octant replication in the map-making translates mainly into a lack of power in the first bin (centered around $\ell = 32$) which is hence discarded in later plots.

4.2 Radio source characterisation

We first investigate the bispectrum dependence on the configurations at a given frequency. We plot the bispectrum in four commonly used configurations, namely equilateral (ℓ, ℓ, ℓ), isosceles orthogonal ($\ell, \ell, \sqrt{2}\ell$), isosceles flat ($\ell, \ell, 2\ell$), and squeezed ($\ell_{\text{min}}, \ell, \ell$) configurations. They furthermore sample rather well the configuration space (see Fig. 1).

We see in Fig. 3, black thick line, that the bispectrum is constant. This result is independent of the frequency. Moreover the value of the constant is independent of the configuration. This is what we expect from white noise and it shows that radio sources are indeed randomly distributed over the sky.

We show in Fig. 4 the dependence with frequency of the bispectrum amplitude averaged over all the configurations, in equivalent temperature unit for the upper panel and flux unit for the bottom panel. The amplitude is maximal at the lowest frequency 30 GHz, it then decreases to become mostly flat above 90 GHz because of free-free emission and inverted spectra sources.

The bispectrum was fitted with the one population prescription described in Sect. 3.2, using the power spectrum extracted from the simulations and the multiplicative constant which minimizes the χ^2 of the observed bispectrum to the prescribed one with error bars from Wick's expansion. The fit of the bispectrum with the prescription is very good: Fig. 5 shows that the relative error (exact to fit) lies in the range between -2% and +2% with a mean relative error always less than 1‰.

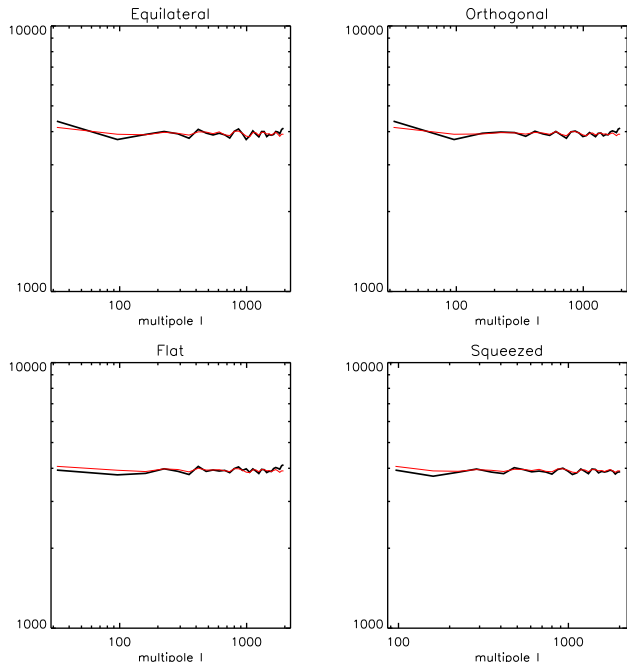


Figure 3. Thick black line: Radio bispectrum at 90 GHz in different configurations: equilateral (ℓ, ℓ, ℓ), isosceles orthogonal ($\ell, \ell, \sqrt{2}\ell$), isosceles flat ($\ell, \ell, 2\ell$), and squeezed ($\ell_{\text{min}}, \ell, \ell$). The red line is the fit with prescription. The unit of the bispectra is $\text{Jy}^3 \cdot \text{sr}^{-1}$

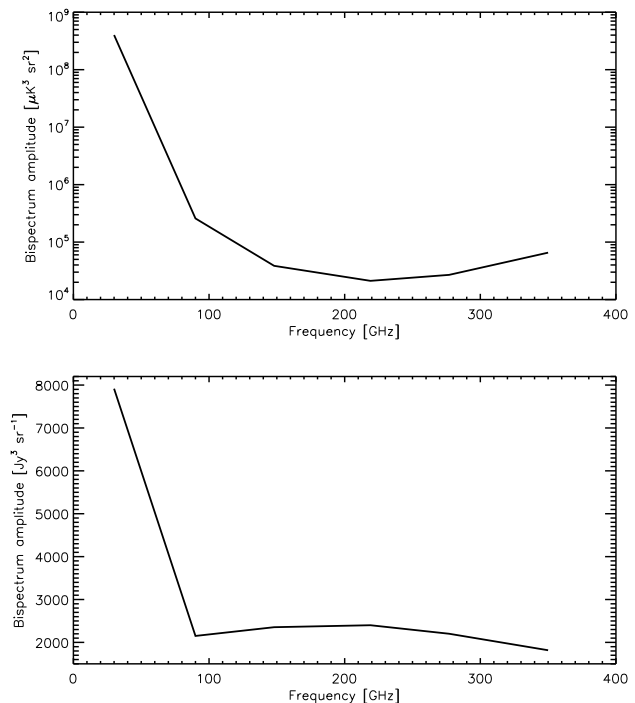


Figure 4. Amplitude of the radio bispectrum at 30, 219, 148, 277, 90, and 350 GHz, in temperature units for the upper panel and flux units for the bottom panel.

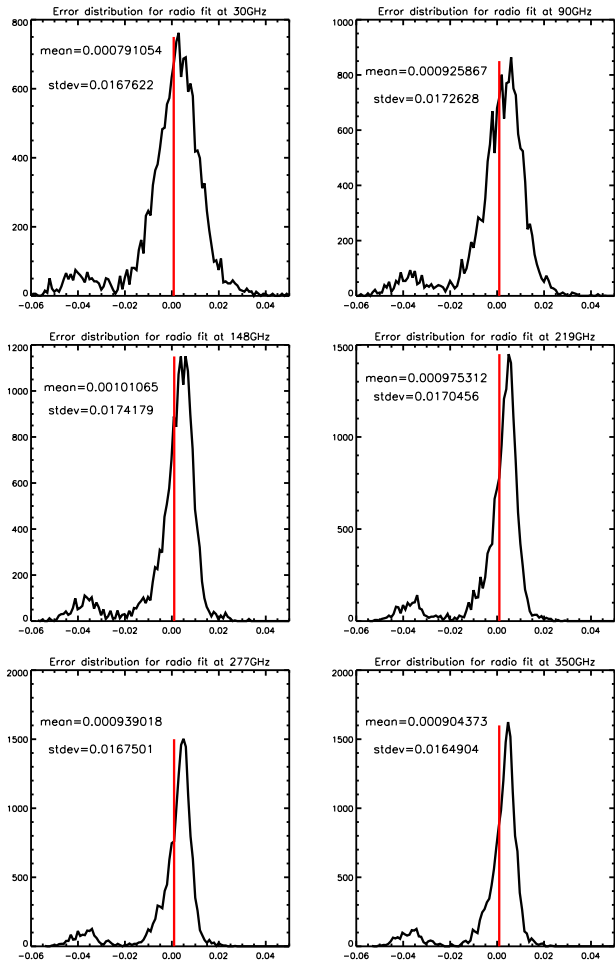


Figure 5. Relative error distribution with the prescription for radio sources alone. The vertical bar shows the mean of the distribution

4.3 IR source characterisation

Figure 6 shows the amplitude of the bispectrum in the equilateral configuration for the different frequencies. Dusty galaxy emission peaks at IR frequencies, and plummets in the radio domain and so does the amplitude of the bispectrum. The bispectrum decreases with ℓ , well fitted by a power-law for $100 \leq \ell \leq 1000$, and with a flattening at higher multipoles. The decrease is expected from the clustering of IR galaxies on large scales. We found that the slopes were about the same for equilateral, flat and orthogonal configurations except for the squeezed triangles. Indeed, for the latter ℓ_1 is fixed, while for the other configurations ℓ_1, ℓ_2, ℓ_3 are all proportional to ℓ .

The flattening of the bispectrum at high multipoles, indicative of the shot-noise contribution, occurs at lower multipoles with increasing frequency (e.g at 350 GHz the bispectrum deviates from a power law at $\ell \sim 1000$ while at 90 GHz it is not before $\ell \sim 1500$). This is explained by the contribution of the high-flux galaxies, in Sehgal et al.’s simulations, that accounts for the shot-noise ($b^{\text{shot}} \sim \int S^3 \frac{dn}{dS} dS$) and at the same time have a steeper emission than the galaxies accounting for the clustering term.

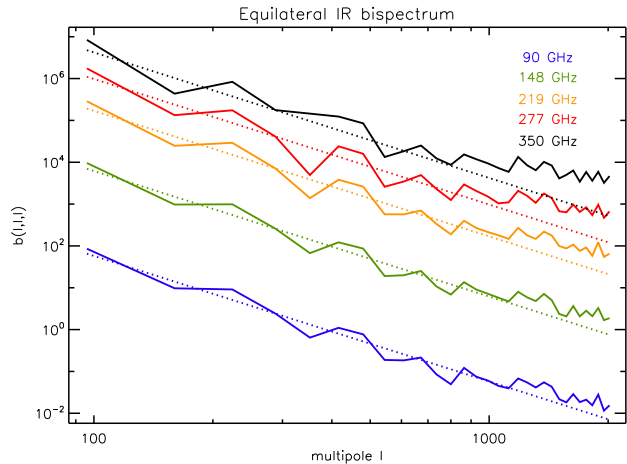


Figure 6. Infrared equilateral bispectrum at 90, 148, 219, 277, and 350 GHz from bottom to top. Dotted corresponding lines are the power-law fit

The bispectrum was fitted with the one population prescription described in Sect. 3.2, using the multiplicative constant which minimizes the χ^2 , as previously for radio sources. We show in Fig. 7 how the bispectrum of the IR sources compares with the prescribed one. We see that the bispectrum obtained with the prescription is good, with a mean relative error always $\leq 10\%$ and a standard deviation $\leq 35\%$, except for the 350 GHz channel.

4.4 Total contribution from IR and radio source populations

We now present the results when the two populations of sources contribute to the signal at the frequencies 30, 90, 148, 219, 277, and 350 GHz. To do so, we simply add the simulated maps at each frequency.

We illustrate the frequency dependence on frequency for one single configuration, namely equilateral, see Fig. 8.

The frequency behaviour is as expected from an independent combination of the IR and RAD bispectra. The radio source contribution dominates at low frequencies 30 and 90 GHz (blue and purple lines) and its bispectrum is flat. Infrared galaxies dominate at the highest frequencies 277 and 350 GHz (black and red upper lines) and show the characteristic power-law dependence due to clustering followed by a flattening of the bispectrum. At intermediate frequencies both populations contribute to the signal. The clustering-induced term of IR-galaxies dominates on large angular scale while the random-noise term of radio-galaxies dominates at small angular scale. The cross-over between radio and IR-galaxy bispectra is shifted to higher ℓ s with increasing frequency. It is worth noting in Fig. 9 that at the lowest multipoles and at highest frequencies, the IR galaxies produce a bispectrum at least 10 times more important than the radio sources.

We illustrate the bispectrum dependence on configurations at 350 GHz, see Fig. 10 thick black line. We note that infrared-radio cross-over occurs at about the same scale for the equilateral, orthogonal and flat configurations, but is at higher ℓ in squeezed configuration. This is expected because

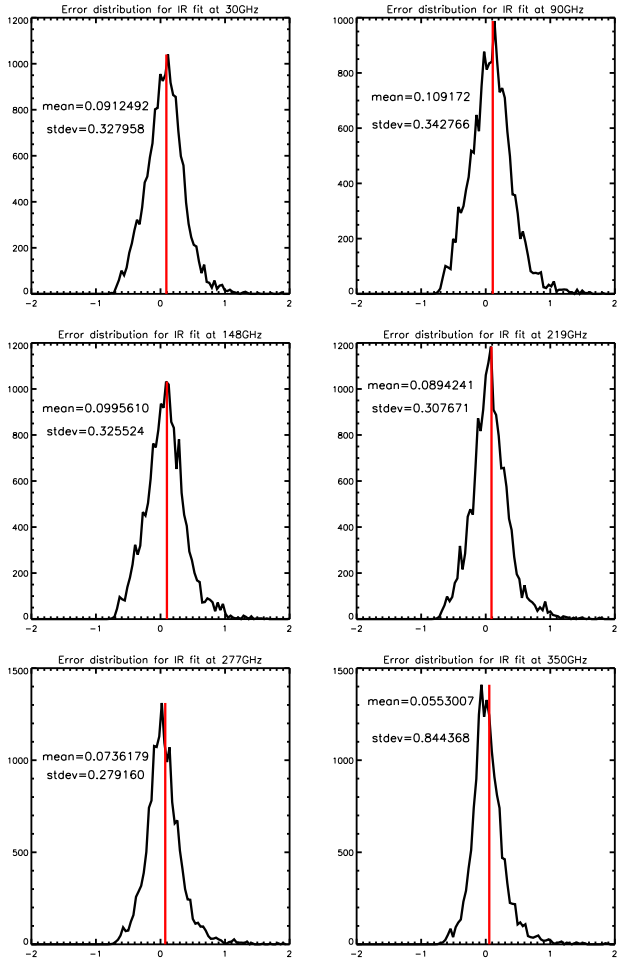


Figure 7. Relative error distribution with the prescription for infrared sources alone. The vertical bar shows the mean of the distribution

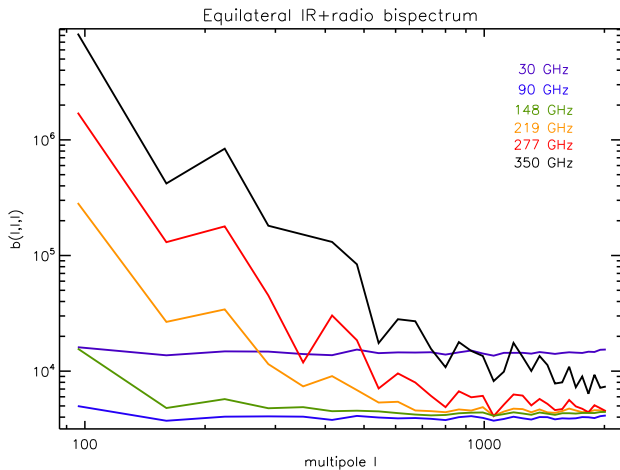


Figure 8. Infrared + radio orthogonal bispectrum at 30, 90, 148, 219, 277, and 350 GHz. The purple flat upper line is 30 GHz, the blue flat lowest line is 90 GHz, more variable decreasing lines from bottom to top are 148, 219, 277, and 350 GHz

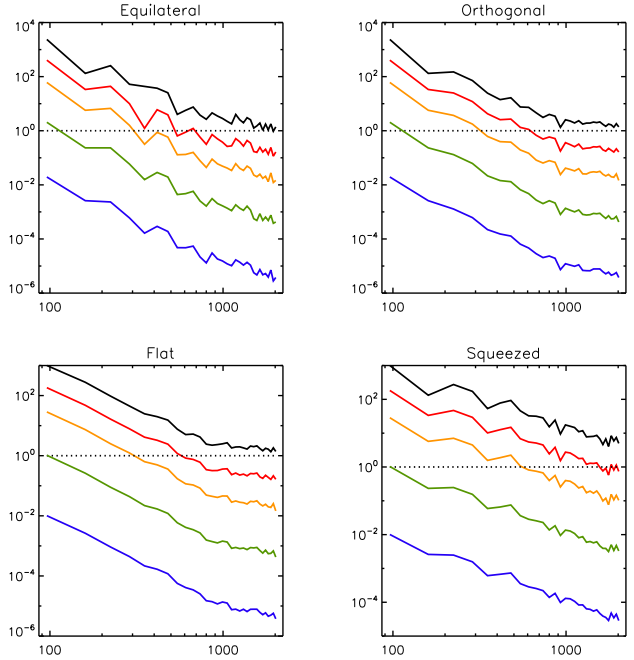


Figure 9. Ratio of the IR bispectrum to the radio one at 90, 148, 219, 277, and 350 GHz from bottom to top. The dotted line indicates equality.

the squeezed IR bispectrum decreases more slowly than other configurations, one of the multipoles being fixed. Figure 10 also displays (thin red line) the bispectrum computed with two-population prescription derived in Sect. 3, i.e. adding up independently the prescription for radio sources and infrared sources derived in the previous sections. This is compared to a bispectrum computation considering only a single population (thin blue line). From Fig. 10, and Fig. 11 showing the distribution of relative errors with respect to these two prescriptions, we see that the two-population prescription performs much better than the single-population prescription. The former captures well the overall shape of the bispectrum and it adjusts particularly well the high l s. As a matter of fact, the mean relative error is lower than 3% up to 350 GHz and the dispersion increases from 1.5% at 30 GHz to 21% at 350 GHz.

As expected, at 30 and 90 GHz the two prescriptions give same results since radio sources totally dominate the signal. At higher frequencies, both the mean errors and the dispersions derived using the two-population prescription are smaller than those obtained with the single-population prescription. Interestingly enough, at the highest frequency (350 GHz) where IR emission from galaxies is dominant, the single-population prescription is not satisfactory. As a matter of fact, configurations with at least one high multipole dominate the distributions (e.g 7/8th of the configurations have at least one $l_i \geq 1000$). At 350 GHz these l s are dominated by infrared shot-noise, so the computation of the prescriptions combine the IR shot noise and radio spectrum which are both flat. The radio emission is subdominant compared to infrared shot-noise but nevertheless not negligible so the single-population prescription leads to an overestimate of the total bispectrum. This is clearly visible

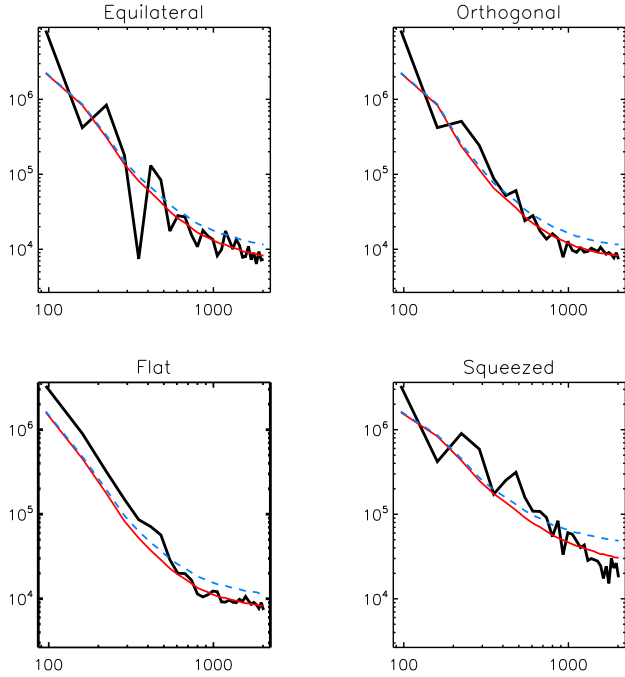


Figure 10. Infrared + radio bispectrum at 350 GHz in different configurations. The thick black line is the computed bispectrum. Smoother solid lines are the fit with prescriptions: the upper blue line with the single-source prescription, and the lower red line with the two-sources prescription.

in Fig. 10 where the single population prescription (blue thin line) is systematically higher than the computed bispectrum (black thick line) and than the two-population prescription (red thin line), particularly at high multipoles.

5 CONSEQUENCES ON NON-GAUSSIANITY MEASURES

5.1 (P, F, S) parametrisation

The (P, F, S) -parametrisation of the bispectrum proposed in Sect. 2.3 allows us to visualise the bispectrum dependence on the configurations. The bispectrum is computed for 32 perimeters in the ℓ space. Only nine perimeters are shown for illustration in Figs. 12 and 13, for the radio and IR-source populations respectively. The bispectrum values are colour coded from blue (lowest value) to red (highest value). The succession of plots, arranged by increasing perimeters, exhibits the allowed configurations at given perimeter with the equilateral configuration being the starting (upper left panel) and ending point (lower right panel). Unsurprisingly the bispectrum amplitude of the radio sources does not vary with the configuration (same color code for all points in Fig. 12). As for the IR sources, Fig. 13, the bispectrum amplitude decreases with perimeter, thus from upper left to lower right panel. Moreover, it is worth noting that the bispectrum values do not vary vertically. This means that within the proposed (P, F, S) -parameterisation the bispectrum of the IR sources is quasi-independent of F , reducing the full bispectrum to a function of the two parameters P and S . Finally, at a given perimeter, i.e. scale, the bispectrum of

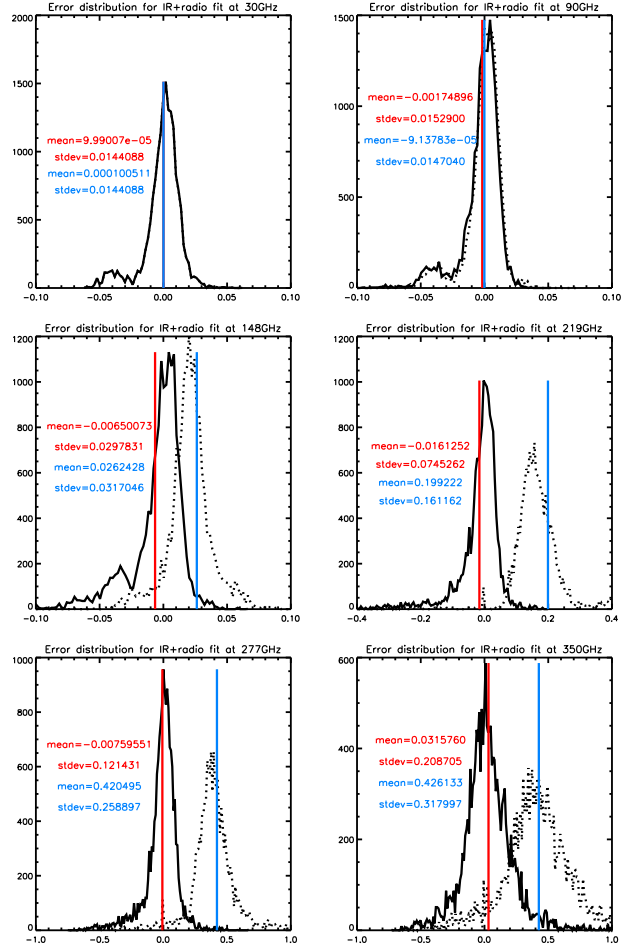


Figure 11. Relative error distribution with the prescriptions for the combination of infrared and radio sources. The dotted line is obtained with the single population prescription, the solid line with the two populations prescription. Vertical bars show the mean of the distribution, red for the single population prescription and blue for the two populations prescription.

the IR sources is more dependent on the configuration and peaks in the squeezed triangles, upper left points in panels 2 to 5.

5.2 point sources contamination to f_{NL}

We now explore the point-source non-Gaussianity in terms of contamination to the f_{NL} estimation. For pedagogical purposes, we consider the SW regime, i.e. a constant transfer function without acoustic oscillations, damping etc.

For IR sources alone, which dominate at high frequencies, $b(\ell_1, \ell_2, \ell_3) \propto \sqrt{C_{\ell_1} C_{\ell_2} C_{\ell_3}}$. Combined with Planck's latest constraints on the CIB $\ell \times C_\ell \simeq \text{const}$ (Planck-Collaboration 2011d), this yields:

$$b^{\text{IR}}(\ell_1, \ell_2, \ell_3) \propto \frac{1}{\sqrt{\ell_1 \ell_2 \ell_3}}$$

which has a similar shape to the local template in the SW limit, Eq. (13). We define the scalar product between the

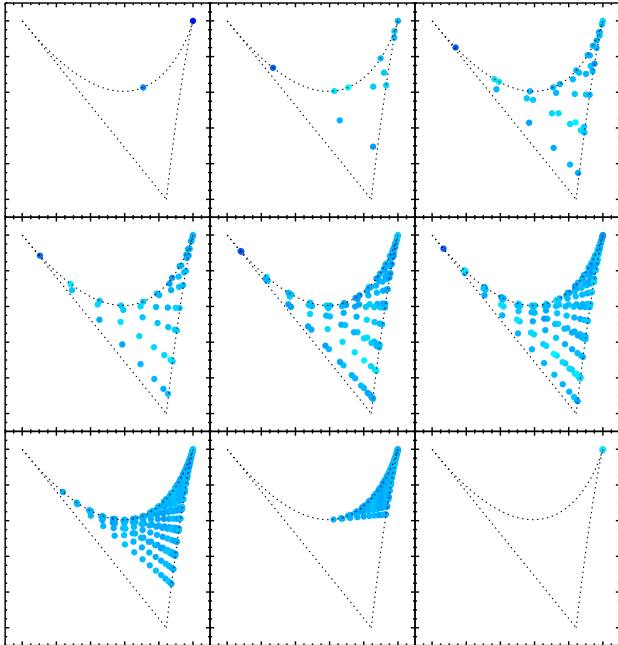


Figure 12. Radio bispectrum in the (P, F, S) parametrisation at 90 GHz. Each plot is a slice of constant perimeter P , the value of the bispectrum is encoded in a logarithmic color scale from violet-blue to red

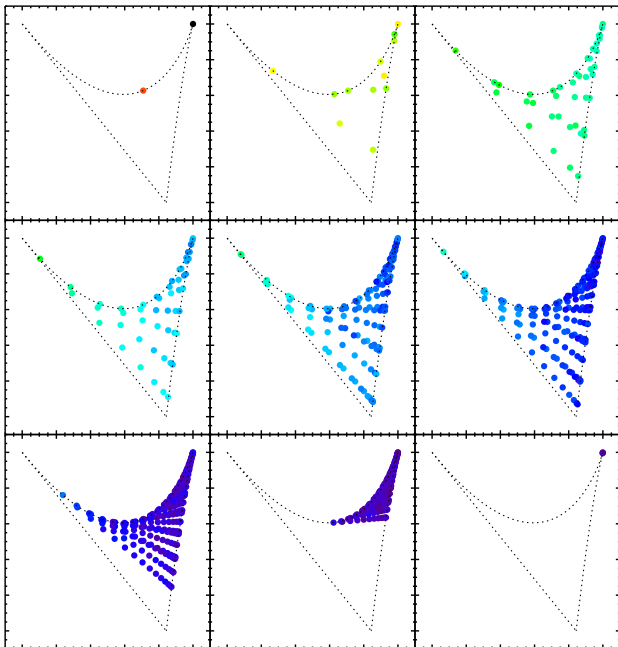


Figure 13. IR bispectrum in the (P, F, S) parametrisation at 148 GHz.

bispectra f, g :

$$\langle f, g \rangle = \sum_{\ell_1 \leq \ell_2 \leq \ell_3} \frac{f(\ell_1, \ell_2, \ell_3) \times g(\ell_1, \ell_2, \ell_3)}{C_{\ell_1}^{\text{CMB}} C_{\ell_2}^{\text{CMB}} C_{\ell_3}^{\text{CMB}}}$$

where the denominator is the variance of the local bispectrum, for triangles with $\ell_1 \neq \ell_2 \neq \ell_3$. The correlation coefficient

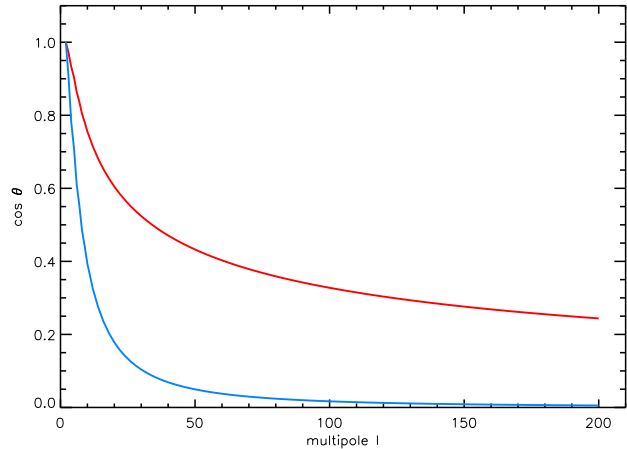


Figure 14. Correlation between SW local bispectrum and respectively IR (red) and radio (blue) bispectrum, as a function of the maximum multipole used ($\ell_{\min} = 2$)

between a bispectrum b^α and the local bispectrum b^{loc} is:

$$\cos \theta_\alpha = \frac{\langle b^\alpha, b^{\text{loc}} \rangle}{\|b^\alpha\| \|b^{\text{loc}}\|}$$

with α being IR or radio.

Figure 14 shows that, for $\ell < 200$, the correlation between radio and local bispectra decreases quickly, so that the two bispectra may be distinguished efficiently. Conversely, even when using a large multipole range, the IR bispectrum is significantly correlated with the local one.

The contribution of the bispectrum of point sources population α to f_{NL} is:

$$\Delta f_{\text{NL}}^\alpha = \frac{\langle b^\alpha, b^{f_{\text{NL}}=1} \rangle}{\langle b^{f_{\text{NL}}=1}, b^{f_{\text{NL}}=1} \rangle} = \frac{\|b^\alpha\|}{\|b^{f_{\text{NL}}=1}\|} \cos \theta_\alpha \quad (30)$$

This equation is the usual bias (Serra & Cooray 2008) of the local-optimised NG estimator, when the local bispectrum has the form of Eq. (13).

A more comprehensive computation of $\Delta f_{\text{NL}}^\alpha$ is achievable by applying the full local estimator described in Sect. 2.2. We built up this estimator using the full transfer function from the latest version of CAMB (Lewis et al. 2000) with WMAP7+BAO+H0 cosmological parameters (Larson et al. 2011), and we tested the estimator on simulations from Elsner & Wandelt (2009). We found the previously noted result that the variance of the estimator increases with f_{NL} . It is unbiased in the range we have tested ($0 \leq f_{\text{NL}} \leq 200$).

We used this f_{NL} estimator on two sets of simulated maps: maps containing all the point sources, and maps with only sources below the flux limit of Planck's Early Release Compact Source Catalogue (ERCSC) (Planck-Collaboration 2011c), namely $S_c = 0.5, 0.5, 0.3, 0.3, 0.3, 0.25$ Jy as a function of frequency. Moreover, we have computed the estimator at three resolutions, ℓ_{\max} , recalibrating the S_{prim} normalisation in each case. Tables 1 and 2 summarise these results.

The bias $\Delta f_{\text{NL}}^{\text{RAD}}$ (see Table 1) is negative on large angular scales, for $\ell_{\max} = 50$. The bias due to radio sources becomes positive at higher multipoles in agreement with Serra & Cooray (2008). This is due to the CMB bispectrum being negative in the SW-dominated regime and the

without flux cut						
ν (GHz)	30	90	148	219	277	350
$\ell_{\max} = 50$	-4.2	-0.0025	-0.00037	-0.00021	-0.00027	-0.00068
$\ell_{\max} = 700$	3850	2.5	0.38	0.21	0.27	0.65
$\ell_{\max} = 2048$	177000	117	18	9.7	12	30
with flux cut						
ν (GHz)	30	90	148	219	277	350
$\ell_{\max} = 700$	108	0.17	0.0071	0.0031	0.0035	0.0064
$\ell_{\max} = 2048$	4930	7.5	0.31	0.14	0.16	0.29

Table 1. Bias on the f_{NL} estimator, $\Delta f_{\text{NL}}^{\text{RAD}}$, due to radio sources

without flux cut						
ν (GHz)	30	90	148	219	277	350
$\ell_{\max} = 50$	$-3.5 \cdot 10^{-8}$	$-5.9 \cdot 10^{-6}$	$-9.2 \cdot 10^{-5}$	-0.0027	-0.023	-1.0
$\ell_{\max} = 700$	$-1.3 \cdot 10^{-6}$	-0.00019	-0.0033	-0.063	-0.55	-9.0
$\ell_{\max} = 2048$	$-1.8 \cdot 10^{-5}$	-0.0026	-0.039	-0.68	-4.8	-67
with flux cut						
ν (GHz)	30	90	148	219	277	350
$\ell_{\max} = 700$	$-1.3 \cdot 10^{-6}$	-0.00019	-0.0033	-0.078	-0.74	-11
$\ell_{\max} = 2048$	$-1.8 \cdot 10^{-5}$	-0.0026	-0.039	-0.67	-6.3	-66

Table 2. Bias of the f_{NL} estimator, $\Delta f_{\text{NL}}^{\text{IR}}$, due to IR sources

radio bispectrum being positive. The bias increases by 5 orders of magnitude at the highest resolution, $\ell_{\max} = 2048$. The reason for the rapid increase of the bias with ℓ_{\max} relates to the weight of the observed bispectrum in Eq. (17), $B_{\ell_1 \ell_2 \ell_3}^{\text{loc}} / C_{\ell_1} C_{\ell_2} C_{\ell_3}$, which rapidly increases with multipole as the product of spectra decreases more quickly than the bispectrum. This leads to a $1/C_\ell$ dependence in squeezed configurations and to a $1/C_\ell^2$ dependence in equilateral configurations. When the observed bispectrum is associated to CMB signal alone, its decrease cancels the increase of the weights so that the sum in Eq. (17) converges. Conversely, the sum diverges when the observed bispectrum is associated with a non-CMB signal and does not decrease with ℓ as fast as the CMB.

The bias $\Delta f_{\text{NL}}^{\text{RAD}}$ is maximal at 30 GHz and rapidly decreases with frequency. It slightly increases again at the two highest frequencies following the amplitude of the bispectrum in temperature units which is plotted in the upper panel of Fig. 4

As shown in Table 1, masking sources above the ERCSC flux limit proves very efficient to significantly decrease the radio contamination to f_{NL} at all the frequencies. At a Planck-like resolution, $\ell_{\max} = 2048$, the bias $\Delta f_{\text{NL}}^{\text{RAD}}$ is reduced below unity above 150 GHz. It is of the order of Planck's expected error bars at 90 GHz. At 30 GHz the bias is still important.

The bias due to IR sources $\Delta f_{\text{NL}}^{\text{IR}}$ is always negative, see Table 2. As a matter of fact, we have shown that the IR bispectrum peaks in squeezed configurations just like the CMB bispectrum and these configurations thus dominate the sum in Eq. (17). Moreover, in the squeezed limit the CMB bispectrum is negative while the IR bispectrum is positive. For the same reason as for radio sources, the bias $\Delta f_{\text{NL}}^{\text{IR}}$ blows up at high multipoles. This is particularly important at a Planck-like resolution, $\ell_{\max} = 2048$, where primordial NG tests will need to carefully handle the contamination by IR sources. The IR sources emission plummets at radio frequen-

cies so that $\Delta f_{\text{NL}}^{\text{IR}}$ is completely negligible below 220 GHz. It becomes of the order of Planck's error bars at 277 GHz and it reaches WMAP's central values for f_{NL} at 350 GHz. At higher frequencies the IR contamination to the bispectrum is likely larger but the contamination from our Galaxy needs to be taken into account as well.

Interestingly, masking sources above the ERCSC flux limit does not diminish $\Delta f_{\text{NL}}^{\text{IR}}$, as most of the IR sources are unresolved and the IR clustering is mostly due to faint sources. Masking may even artificially boost $\Delta f_{\text{NL}}^{\text{IR}}$, for example at 277 GHz, since it mostly affects the flat shot-noise which produces a positive bias Δf_{NL} .

6 CONCLUSIONS AND DISCUSSION

We have studied the non-Gaussianity produced by point sources in the frequency range of the CMB from 30 to 350 GHz. We have developed a simple and accurate prescription to infer the bispectrum from the power spectrum for point sources. We have proposed a recipe to derive bispectra out of spectra considering different independent populations of sources, with or without clustering.

Using available all-sky simulations of radio and IR sources we have computed the full-sky binned bispectra for these two populations of sources. We have compared the measured bispectra to those predicted from our prescription and found a very good agreement between the two. We have displayed the bispectrum using a new parametrisation which highlights efficiently the configuration dependence.

Using the simulations of IR and radio sources, we have characterised their bispectrum, showing the configuration dependence and the frequency behaviour. In particular and for the first time, we showed that the IR bispectrum peaks in the squeezed triangles and that the clustering of IR sources enhances the bispectrum values by several orders of magnitude on large angular scales $\ell \sim 100$. The bispectrum of IR sources starts to dominate over that of radio sources on large angular scales at 150 GHz, and it dominates over the whole multipole range at 350 GHz.

Finally to illustrate the contamination by point sources of local CMB non-Gaussianity, we derive the bias on f_{NL} induced by radio and IR sources, for WMAP or Planck-like angular resolutions. Radio sources produce a positive bias which is significantly reduced ($\Delta f_{\text{NL}} < 1$ for $\nu \geq 150$ GHz) by masking the sources above a given flux limit taken as the ERCSC cut. The form of the IR bispectrum mimics a primordial 'local' bispectrum f_{NL} on large angular scales. The IR sources produce a negative bias which becomes important for Planck-like resolution and at high frequencies ($\Delta f_{\text{NL}} \sim -6$ at 277 GHz and $\Delta f_{\text{NL}} \sim -60-70$ at 350 GHz). Most of the signal is associated with the clustering of faint IR sources. Therefore, the bias $\Delta f_{\text{NL}}^{\text{IR}}$ is not reduced by masking sources above a flux limit but, in some cases, even increased due to the reduction of the shot-noise term.

Our analysis highlights the sensitivity of the bias on f_{NL} to the experiment properties (maximum resolution and frequency range), to the point-source models (clustering or no, resolved or not) and to their scale dependence with respect to the CMB. For high resolution high frequency CMB experiments, primordial NG estimations need to take special care of astrophysical contaminations; ultimately leading to

a simultaneous measure of the primordial and astrophysical non-Gaussianity.

ACKNOWLEDGMENTS

The authors acknowledge the use of Lambda archive⁴, CAMB (Lewis et al. 2000) and the HEALPix (Gorski et al. 2005) package. They made use of all-sky simulations of the microwave sky by Sehgal et al. (2010) and non-Gaussian CMB simulations by Elsner & Wandelt (2009). They wish to thank S. Ilic, G. Lagache and A. Penin for useful discussions. NA and FL thank Université de Genève and the Swiss NSF for partial support and hosting, MK and MF thank the IAS for hospitality on numerous occasions. The authors acknowledge partial support from PHC Germaine de Staël. FL further acknowledges financial support from a PhD fellowship of the Ecole Normale Supérieure Paris. MK and MF acknowledge funding by the Swiss NSF. Part of the calculations for this paper were performed on the *Andromeda* cluster of the Université de Genève.

APPENDIX A: CLUSTERED SOURCES SHOT-NOISE

A source with flux S enclosed in a pixel Ω_{pix} yields a rise of temperature compared to the CMB:

$$\Delta T = \frac{S}{\Omega_{\text{pix}}} \times \underbrace{\frac{(e^x - 1)^2}{x^2 e^x}}_{\equiv k_\nu} \times \frac{c^2}{2\nu^2 k_B} \quad (\text{A1})$$

where $x = h\nu/k_B T_{\text{CMB}}$ and $k_\nu = \left. \frac{\partial B(\nu, T)}{\partial T} \right|_{T_{\text{CMB}}}$.

The two-point correlation function of point sources takes the form:

$$\langle \Delta T(\mathbf{n}) \Delta T(\mathbf{n}') \rangle = F(\mathbf{n}, \mathbf{n}') + \Gamma \delta_{\mathbf{n}, \mathbf{n}'}$$

where $F(\mathbf{n}, \mathbf{n}')$ is the correlation function coming from the spatial distribution of the sources, and the Kronecker term comes from the discreteness of the sources:

$$\Gamma = \langle \Delta T^2 \rangle - F(\mathbf{n}, \mathbf{n})$$

Assuming statistical isotropy, we get:

$$C_\ell = C_\ell^{\text{clust}} + C_\ell^{\text{shot}} \quad \text{with} \quad C_\ell^{\text{shot}} = \Gamma \Omega_{\text{pix}}$$

Indeed:

$$\begin{aligned} \langle a_{\ell m} a_{\ell' m'}^* \rangle &= \int d^2 \mathbf{n} d^2 \mathbf{n}' Y_{\ell m}(\mathbf{n}) Y_{\ell' m'}^*(\mathbf{n}') \langle \Delta T(\mathbf{n}) \Delta T(\mathbf{n}') \rangle \\ &= \underbrace{\int d^2 \mathbf{n} d^2 \mathbf{n}' Y_{\ell m}(\mathbf{n}) Y_{\ell' m'}^*(\mathbf{n}') F(\mathbf{n}, \mathbf{n}')}_{= C_\ell^{\text{clust}} \delta_{\ell \ell'} \delta_{m m'}} \\ &\quad + \sum_{\mathbf{n}_i, \mathbf{n}'_j} Y_{\ell m}(\mathbf{n}_i) Y_{\ell' m'}^*(\mathbf{n}'_j) \times \Gamma \delta_{\mathbf{n}_i, \mathbf{n}'_j} \Omega_{\text{pix}}^2 \\ &= C_\ell^{\text{clust}} \delta_{\ell \ell'} \delta_{m m'} + \Gamma \Omega_{\text{pix}} \sum_{\mathbf{n}_i} Y_{\ell m}(\mathbf{n}_i) Y_{\ell' m'}^*(\mathbf{n}_i) \Omega_{\text{pix}} \\ &= C_\ell^{\text{clust}} \delta_{\ell \ell'} \delta_{m m'} + \Gamma \Omega_{\text{pix}} \int d^2 \mathbf{n} Y_{\ell m}(\mathbf{n}) Y_{\ell' m'}^*(\mathbf{n}) \\ &\quad = C_\ell^{\text{clust}} \delta_{\ell \ell'} \delta_{m m'} + \Gamma \Omega_{\text{pix}} \delta_{\ell \ell'} \delta_{m m'} \quad (\text{A2}) \end{aligned}$$

C_ℓ has units $\mu K^2 \cdot \text{sr}$. Let us number by $i=1..N$ all sources of the sky, then the temperature of a pixel is given by:

$$\Delta T(\mathbf{n}) = \frac{k_\nu}{\Omega_{\text{pix}}} \sum_{i=1}^N S_i \times \mathbb{1}_{[i \in \mathbf{n}]} \quad (\text{A3})$$

where $\mathbb{1}_{[i \in \mathbf{n}]}$ is 1 if the source i is in the pixel and 0 otherwise. We have:

$$\langle \mathbb{1}_{[i \in \mathbf{n}]} \rangle = 1/n_{\text{pix}}$$

Hence for $\mathbf{n} \neq \mathbf{n}'$:

$$\begin{aligned} F(\mathbf{n}, \mathbf{n}') &= \langle \Delta T(\mathbf{n}) \Delta T(\mathbf{n}') \rangle \\ &= \frac{k_\nu^2}{\Omega_{\text{pix}}^2} \langle \sum_{i \neq j} S_i S_j \times \mathbb{1}_{[i \in \mathbf{n}]} \mathbb{1}_{[j \in \mathbf{n}']} \rangle \end{aligned}$$

Then we find:

$$\begin{aligned} \langle \Delta T(\mathbf{n})^2 \rangle &= \frac{k_\nu^2}{\Omega_{\text{pix}}^2} \langle \sum_{i,j=1}^N S_i S_j \times \mathbb{1}_{[i \in \mathbf{n}]} \mathbb{1}_{[j \in \mathbf{n}]} \rangle \\ &= \frac{k_\nu^2}{\Omega_{\text{pix}}^2} \langle \sum_{i \neq j} S_i S_j \times \mathbb{1}_{[i \in \mathbf{n}]} \mathbb{1}_{[j \in \mathbf{n}]} \rangle \\ &\quad + \frac{k_\nu^2}{\Omega_{\text{pix}}^2} \sum_{i=1}^N S_i^2 \times \langle \mathbb{1}_{[i \in \mathbf{n}]} \rangle \\ &= \lim_{\mathbf{n} \rightarrow \mathbf{n}'} \langle \Delta T(\mathbf{n}) \Delta T(\mathbf{n}') \rangle + \frac{k_\nu^2}{\Omega_{\text{pix}}^2} \frac{1}{n_{\text{pix}}} \sum_{\text{sources}} S^2 \end{aligned}$$

Recalling $\Omega_{\text{pix}} = \frac{4\pi}{n_{\text{pix}}}$ and introducing $\frac{dn}{dS}$ the number counts of sources

$$\langle \Delta T(\mathbf{n})^2 \rangle = F(\mathbf{n}, \mathbf{n}) + \underbrace{\frac{k_\nu^2}{4\pi \Omega_{\text{pix}}} \int S^2 \frac{dn}{dS}}_{= \Gamma} dS$$

And finally:

$$C_\ell^{\text{shot}} = \Gamma \Omega_{\text{pix}} = \frac{k_\nu^2}{4\pi} \int S^2 \frac{dn}{dS} dS \quad (\text{A4})$$

which is the shot-noise formula Eq. 19.

The integrals runs from $S=0$ to S_{cut} the flux detection limit of the survey, ie sources with $S > S_{\text{cut}}$ have been removed. Note that this result is independent of the two-point correlation function, which we did not specify.

At order 3 for the bispectrum, the computation is a bit more involved but follows the same line, and we find:

$$\langle a_{\ell_1 m_1} a_{\ell_2 m_2} a_{\ell_3 m_3} \rangle = G_{\ell_1 \ell_2 \ell_3}^{m_1 m_2 m_3} \times b_{\ell_1 \ell_2 \ell_3} \quad (\text{A5})$$

⁴ http://lambda.gsfc.nasa.gov/toolbox/tb_cmb_sim_ov.cfm

with

$$b_{\ell_1 \ell_2 \ell_3}^{\text{shot}} = \frac{k_\nu^3}{4\pi} \times \int S^3 \frac{dn}{dS} dS \quad (\text{A6})$$

which is the shot-noise formula Eq. 20.

References

- Aghanim N., Kunz M., Castro P., Forni O., 2003, *Astron.Astrophys.*, 406, 797
- Aghanim N., Majumdar S., Silk J., 2008, *Reports on Progress in Physics*, 71, 066902
- Amblard A., Cooray A., Serra P., et al. 2011, *Nature*, pp 1–34
- Argueso F., GonzalezNuevo J., Toffolatti L., 2003, *The Astrophysical Journal*, 598, 86
- Babich D., Pierpaoli E., 2008, *Physical Review D*, 77
- Barrientos L. F., Battistelli E. S., Bond J. R., Brown B., Burger B., Chervenak J., 2010, arXiv:1009.0847v1
- Bucher M., Tent B. V., Carvalho C. S., 2010, *Monthly Notices of the Royal Astronomical Society*, 000
- Byrnes C. T., Choi K.-Y., 2010, *Advances in Astronomy*, 2010, 1
- Cooray A., Kesden M., 2002, *New Astronomy*, 8, 21
- Creminelli P., Nicolis A., Senatore L., Tegmark M., Zaldarriaga M., 2006, *Journal of Cosmology and Astroparticle Physics*, 2006, 004
- Creminelli P., Zaldarriaga M., 2004, *Journal of Cosmology and Astroparticle Physics*, 2004, 006
- De Troia G., Ade P., Bock J., Bond J., Boscaleri A., et al., 2003, *Mon.Not.Roy.Astron.Soc.*, 343, 284
- de Zotti G., Ricci R., Mesa D., Silva L., Mazzotta P., Toffolatti L., González-Nuevo J., 2005, *Astronomy and Astrophysics*, 431, 893
- Elsner F., Wandelt B. D., 2009, *The Astrophysical Journal Supplement Series*, pp 1–18
- Fergusson J. R., Liguori M., 2010, arXiv:1006.1642, pp 1–30
- Gorski K., Hivon E., Banday A., Wandelt B., Hansen F., et al., 2005, *Astrophys.J.*, 622, 759
- Hall N. R., Keisler R., Knox L., et al. 2010, *The Astrophysical Journal*, 718, 632
- Hicken M., Wood-Vasey W. M., Blondin S., Challis P., Jha S., Kelly P. L., Rest A., Kirshner R. P., 2009, *The Astrophysical Journal*, 700, 1097
- Keisler R., Reichardt C. L., Aird K. A., et al. 2011, arXiv:1105.3182v1
- Komatsu E., Dunkley J., Nolte M. R., Bennett C. L., Gold B., Hinshaw G., Jarosik N., Larson D., Limon M., Page L., Spergel D. N., Halpern M., Hill R. S., Kogut A., Meyer S. S., Tucker G. S., Weiland J. L., Wollack E., Wright E. L., 2009, *The Astrophysical Journal Supplement Series*, 180, 330
- Komatsu E., Smith K. M., Dunkley J., Bennett C. L., Gold B., Hinshaw G., Jarosik N., Larson D., Nolte M. R., Page L., Spergel D. N., Halpern M., Hill R. S., Kogut a., Limon M., Meyer S. S., Odegard N., Tucker G. S., Weiland J. L., Wollack E., Wright E. L., 2011, *The Astrophysical Journal Supplement Series*, 192, 18
- Komatsu E., Spergel D. N., 2001, *Phys.Rev.*, D63, 063002
- Komatsu E., Spergel D. N., Wandelt B. D., 2005, *The Astrophysical Journal*, 634, 14
- Kunz M., Banday A. J., Castro P. G., Ferreira P. G., Górski K. M., 2001, *The Astrophysical Journal*, 563, L99
- Lagache G., Bavouzet N., Fernandez-Conde N., Ponthieu N., Rodet T., Dole H., Miville-Deschênes M.-a., Puget J.-L., 2007, *The Astrophysical Journal*, 665, L89
- Lagache G., Puget J. L., 2000, *Astronomy & Astrophysics*, 355, 17
- Larson D., Dunkley J., Hinshaw G., Komatsu E., Nolte M. R., Bennett C. L., Gold B., Halpern M., Hill R. S., Jarosik N., Kogut a., Limon M., Meyer S. S., Odegard N., Page L., Smith K. M., Spergel D. N., Tucker G. S., Weiland J. L., Wollack E., Wright E. L., 2011, *The Astrophysical Journal Supplement Series*, 192, 16
- Lesgourgues J., 2011, arXiv:1104.2932
- Lewis A., Challinor A., Lasenby A., 2000, *The Astrophysical Journal*, 538, 473
- Liddle A. R., Lyth D. H., 2000, *Cosmological Inflation and Large-Scale Structure*. Cambridge University Press
- Low F. J., Tucker W. H., 1968, *Physical Review Letters*, 21, 1538
- Maldacena J., 2003, *Journal of High Energy Physics*, 2003, 013
- Matsuhara H., Kawara K., Sato Y., Taniguchi Y., Okuda H., Matsumoto T., Sofue Y., Wakamatsu K., Cowie L. L., 2000, *Astronomy & Astrophysics*, 361, 407
- Munshi D., Valageas P., Cooray A., Heavens A., 2009, *Monthly Notices of the Royal Astronomical Society*, 000, 1
- Percival W. J., Reid B. A., Eisenstein D. J., et al. 2010, *Monthly Notices of the Royal Astronomical Society*, 401, 2148
- Planck-Collaboration 2011a, arXiv:1101.2047
- Planck-Collaboration 2011b, arXiv:1101.2044
- Planck-Collaboration 2011c, arXiv:1101.2041
- Planck-Collaboration 2011d, arXiv:1101.2028
- Puget J.-L., Abergel A., Bernard J.-P., Boulanger F., Burton W. B., Desert F.-X., Hartmann D., 1996, *Astronomy & Astrophysics*, 308, 5
- Riess A. G., Macri L., Casertano S., Sosey M., Lampeitl H., Ferguson H. C., Filippenko A. V., Jha S. W., Li W., Chornock R., Sarkar D., 2009, *The Astrophysical Journal*, 699, 539
- Righi M., Hernández-Monteagudo C., Sunyaev R. A., 2008, *Astronomy and Astrophysics*, 478, 685
- Sehgal N., Bode P., Das S., Hernandez-Monteagudo C., Huffenberger K., Lin Y.-T., Ostriker J. P., Trac H., 2010, *The Astrophysical Journal*, 709, 920
- Seljak U., Zaldarriaga M., 1996, *The Astrophysical Journal*, 469, 437
- Serra P., Cooray A., 2008, *Physical Review D*, 77, 1
- Smoot G. F., Bennett C. L., Kogut A., et al. 1992, *The Astrophysical Journal*, 396, L1
- Spergel D., Goldberg D., 1999, *Physical Review D*, 59, 1
- Viero M. P., Ade P. a. R., Bock J. J., et al. 2009, *The Astrophysical Journal*, 707, 1766